Liu *et al. Microstructures* 2024;4:2024015
DOI: 10.20517/microstructures.2023.91

Microstructures

Research Article

Open Access

Pressure-induced superconductivity in hypercoordinated 5*p*-block element nitrides MN_6 (M = Sb, Te, I)

Yan Liu[1], Da Li[1], Tian Cui[1,2]

[1]State Key Laboratory of Superhard Materials, College of Physics, Jilin University, Changchun 130012, Jilin, China.
[2]School of Physical Science and Technology, Ningbo University, Ningbo 315211, Zhejiang, China.

Correspondence to: Prof. Da Li, State Key Laboratory of Superhard Materials, College of Physics, Jilin University, 2699 Qianjin Street, Changchun 130012, Jilin, China. E-mail: dali@jlu.edu.cn; Prof. Tian Cui, School of Physical Science and Technology, Ningbo University, 818 Fenghua Road, Ningbo 315211, Zhejiang, China. E-mail: cuitian@nbu.edu.cn

How to cite this article: Liu Y, Li D, Cui T. Pressure-induced superconductivity in hypercoordinated 5*p*-block element nitrides MN_6 (M = Sb, Te, I). *Microstructures* 2024;4:2024015. https://dx.doi.org/10.20517/microstructures.2023.91

Received: 19 Dec 2023 **First Decision:** 30 Jan 2024 **Revised:** 4 Feb 2024 **Accepted:** 1 Mar 2024 **Published:** 27 Mar 2024

Academic Editor: Liangzhi Kou **Copy Editor:** Pei-Yun Wang **Production Editor:** Pei-Yun Wang

Abstract

The recent studies of high-pressure synthesis and stabilization of a variety of polynitrogens have had an immense impact on nitrogen chemistry. However, the metallization and superconductivity of solid nitrogen at high pressure have not yet been verified. Here, based on first-principles calculations, we report a remarkable finding of the metallic N_6 hexazine ring stabilized in the 5*p*-block element nitrides MN_6 (M = Sb, Te, I) at an experimentally accessible pressure of 100 GPa. Strikingly, the 5*p*-block elements act as precompressors and electron donors for the N sublattice, leading to the Jahn-Teller distortion of the N_6 hexazine ring and endowing the 5*p*-block element nitrides superconductivity with a high superconducting critical temperature (T_c) of up to 36.8 K, close to the McMillan limit (40 K). This is the first discovery of a nitrogen-based superconductor with distorted N_6 hexazine rings. The high T_c is attributed to the strong electron-phonon coupling that is induced by the phonon softening and the hybridized electronic states between N and 5*s* and 5*p* orbitals of 5*p*-block elements. Our works have broad implications for enriching novel *p*-block element nitrides and nitrogen chemistry under extreme conditions.

Keywords: First-principles, high pressure, crystal structure prediction, nitrides, superconductivity

INTRODUCTION

The metallization of nitrogen (N) has long been considered particularly challenging due to extreme stability of triple-bonded molecular nitrogen. However, over the past 20 years, it has been shown that the physical and chemical properties of nitrogen significantly change at high pressure[1,2]. The outer-shell electrons of nitrogen tend to delocalize upon strong compression, which directly leads to the dissociation of molecular nitrogen to form more close-packed polynitrogen structures[3-6]. Theoretically, pressure-induced nonmetal-to-metal transition in solid nitrogen has been predicted, including the layered black phosphorus phase[7], the *cis-trans* and *Cmcm* chain structures[5,8], and a potentially superconducting *Pnnm* phase[9]. Unfortunately, all the predicted metallic nitrogen phases are metastable structures. Thus far, the metallization of solid nitrogen at high pressure has not yet been verified, although a transition from insulating to conducting has been experimentally demonstrated in dense fluid nitrogen above 125 GPa and 2,500 K[10,11].

Nitrogen-rich compounds provide an alternative route to the synthesis of solid nitrogen[12-17]. In particular, various polynitrogen structures occur as a result of the interaction between secondary element and nitrogen under high pressure, which are stabilized in the form of polyanion and result in the anion-driven metallicity. Consequently, Aslandukov *et al.* synthesized two metallic YN_6 and Y_2N_{11} with unique N_{18} macrocycle and polynitrogen double helix structure at 100 GPa and 3,000 K in a laser-heated diamond anvil cell (DAC)[18]. Conjugated polymeric nitrogen chains and dumbbell units were identified in rhenium nitride ReN_{10} and Re_2N_4, exhibiting metallicity properties[19]. The single-bond nitrogen framework and dinitrogen units were stabilized in metallic TaN_5 and WN_{10}[20,21]. Obviously, anion-driven metallicity has been a regular phenomenon for high-pressure nitrides, except for the transition metal nitrides; it is mainly focused on the alkali metal and alkali earth metal element nitrides[22-24]. Worth noting is that the planer N_6 hexazine rings have been predicted several times in alkali metal and alkali earth metal nitrogen-rich compounds, such as LiN_3, KN_3, RbN_3, and BaN_6[25-28]. Following the theoretical research, Wang *et al.* successfully prepared metallic planar N_6 hexazine dianions that stabilized in K_2N_6[29]. Recently, Laniel *et al.* realized the synthesis of the plane aromatic hexazine N_6 anion in the metallic structure of high-pressure potassium nitrogen compound K_9N_{56}[30].

Compared with the anion-driven metallicity in binary metal-nitrogen compounds of alkali, alkaline earth, and transition metal elements, the high-pressure chemistry and physical properties of *p*-block element nitrides are quite different. Although the metallic and even superconductive B_4N, PN_3, SN_4, and SeN_3 have been theoretically predicted[31-34], the strong electronegativity[35] of the *p*-block elements makes them prone to form covalent bonding with nitrogen. For this reason, the conventional wisdom holds that *p*-block element nitrides are undesirable for developing polymeric nitrogen framework topologies[15]. However, high pressure enables a direct interaction of N_2 and Xe (5*p*-block element) to form XeN_6 with a three-dimensional covalent bonding network, in which the N atoms are polymerized into a chair-like N_6 hexazine ring, but unfortunately, it exhibits non-metallicity[36]. Therefore, other candidate *p*-block elements need to be explored for enlarging and enriching metallic nitrogen structures under compression. Antimony (Sb), tellurium (Te), and iodine (I), as typical 5*p*-block elements, have large atom sizes and moderate electronegativity, which makes them distinct from the lighter *p*-block elements and allows them to coordinate with more atoms at high pressure[37-39]. Furthermore, flexible electronic properties can provide a unique bonding environment, making Sb, Te, and I anticipated to be ideal candidates for inducing novel nitrogen structures with metallicity.

Herein, we introduce a new class of 5*p*-block element nitrides with novel structure and exotic properties. An extensive structure prediction at high pressure was performed using the CALYPSO code, and we uncovered a nitrogen-based superconductor MN_6 (M = Sb, Te, I) with distorted N_6 hexazine rings and

hypercoordinated features. Under high pressure, the vacant 5*d* orbitals of the 5*p*-block elements become valence orbitals and participate in the covalent bonding with N atoms. First-principles calculations for different 5*p*-block element nitrides MN_6 predict diverse T_c values among the same stoichiometry, in which TeN_6 has a noteworthy T_c of 36.8 K at 100 GPa. Crucially, we reveal the superconducting mechanism of 5*p*-block element nitrides. High T_c is attributed to the strong electron-phonon coupling (EPC) derived from the phonon softening and the hybridized electronic states between N and 5*s* and 5*p* orbitals of 5*p*-block elements, while the pressure-induced 5*d* electron is negatively correlated with the superconductivity.

METHODS

Structural optimization and total energy calculation were based on density functional theory (DFT) with the implementation of the Vienna ab initio simulation (VASP) code[40,41]. The exchange-correlation functional was given by Perdew-Burke-Ernzerhof (PBE)[42] of generalized gradient approximation (GGA)[43]. Electron-ion interactions were represented employing the all-electron projector augmented wave (PAW) method[44] with $5s^25p^3$ valence configurations for Sb, $5s^25p^4$ for Te, $5s^25p^5$ for I, and $2s^22p^3$ for N. Electronic wavefunctions were expanded using a plane wave basis set with a cutoff of 520 eV. Monkhorst-Pack grids were generated per cell with a reciprocal space resolution of $2\pi \times 0.03$ Å^{-1}, ensuring that the enthalpy calculations converged to better than 1 meV per atom. Electron localization function (ELF) was calculated by VASP and displayed by the Visualization for electronic and structural analysis (VESTA)[45]. Ab initio molecular dynamics (AIMD) simulations within the canonical ensemble (*NVT*) were used to examine the thermal stability at 300 K and 1,000 K for 5,000 fs[46]. Chemical bonding analyses were carried out using the crystal orbital Hamilton population (COHP) as implemented in the LOBSTER package[47]. The three-dimensional Fermi surface (FS) was depicted using the FermiSurfer software[48].

Phonon dispersion and EPC calculation were performed with the Quantum-ESPRESSO package[49], where the structure is fully re-optimized from the results of PAW. Based on convergence tests, we adopted an appropriate kinetic energy cutoff of 80 Ry and a 12 × 12 × 12 Monkhorst-Pack mesh for Brillouin zone integration. The ultrasoft pseudopotentials of Sb, Te, I, and N were used. Phonon dynamic matrix elements were performed in the first Brillouin zone on a 6 × 6 × 6 *q*-mesh. To ensure the convergence of the EPC matrix elements for the electron-phonon interaction coefficients, a large 24 × 24 × 24 *q*-mesh was required. Here, The EPC parameter λ can be defined as the first reciprocal moment of the spectroscopic function $\alpha^2F(\omega)$[50]:

$$\alpha^2 F(\omega) = \frac{1}{2\pi N(\varepsilon_F)} \sum_{qj} \frac{\gamma_{qj}}{\omega_{qj}} \delta(\hbar\omega - \hbar\omega_{qj}),$$

$$\lambda = 2\int_0^\infty \frac{\alpha^2 F(\omega)}{\omega} d\omega,$$

where $\boldsymbol{q}$ is a wavevector in the first Brillouin zone, j is the phonon mode label, and ω_{qj} is the phonon frequency of mode $\boldsymbol{q}j$. Other important frequency moments are defined as:

$$\omega_{\log} = \exp\left[\frac{2}{\lambda}\int_0^{\infty}\frac{d\omega}{\omega}\alpha^2 F(\omega)\ln\omega\right],$$

$$\langle\omega^2\rangle = \frac{2}{\lambda}\int_0^{\infty}\omega\alpha^2 F(\omega)d\omega,$$

where the $\omega_{\log}$ is the logarithmic average phonon frequency, and $\langle\omega^2\rangle$ represents the average phonon frequency.

RESULTS AND DISCUSSION

Extensive structure searches were performed in binary 5*p*-block element nitrides M_xN_y (M = Sb, Te, I) with different stoichiometric ratios to predict stable structures[51,52], ultimately focusing on the most characteristic nitrogen-rich compounds MN_6 at 100 GPa. Detailed descriptions and results for the structure prediction are displayed in Supplementary computational details, Supplementary Figure 1 and Table 1. Conspicuous in the predicted crystal structure of the 5*p*-block element nitrides MN_6 is the chair-like N_6 hexazine ring, which crystallizes in a rhombohedral primitive cell with *R*3*m* space group symmetry [Figure 1A and B]. The 5*p*-block elements are occupied at the vertex position of the primitive cell and hypercoordinated with twelve N atoms from eight hexazine N_6 rings to form an MN_{12} icosahedral cage [Figure 1C], which is the building block in the construction of the three-dimensional crystal structure. Within the chair-like N_6 hexazine ring, N atoms adopt sp^3 hybridization to form a fourfold coordination structure, which is substantially different from the typical sp^2 hybridization caused by the alternating single-double bonding patterns on well-known hypothetical planar N_6 hexazine ring[53,54]. The structural stability of 5*p*-block element nitrides MN_6 was preliminarily verified by elastic constants calculation [Supplementary Table 2] and molecular dynamic simulation [Supplementary Figure 2]. Subsequently, we focus our analyses mainly on TeN_6 to exhibit its prominent properties while also discussing crucial data and change trends involving other MN_6 compounds.

We first examine the high-pressure electronic structure and chemical bonding of TeN_6. As shown in Figure 2A, the contour plots of the ELF are projected on the (111) plane, cutting through the center of the N_6 hexazine ring. Regions with ELF values of 0.85 are found to localize between N atoms in the N_6 hexazine ring, showing evidence for N–N covalent bonding. A hypothetical N_6 hexazine ring structure (Te_0N_6) is constructed by removing Te from the lattice of TeN_6 and leaving the N sublattice unchanged. Compared with the ELF of TeN_6, the original lone electron pairs of N in the hypothetical N_6 hexazine ring [Figure 2A, middle] collapse and form covalent bonding with Te atoms, which is extremely similar to that of N in XeN_6[36]. Intriguingly, the chair-like N_6 hexazine ring transforms into a planar ring after structural relaxation but remains in the original N sublattice [Figure 2A, right], directly proving that the introduction of 5*p*-block element Te causes structural distortion of the N_6 hexazine ring. A covalent interaction with an ELF of 0.89 between the N atoms in the planar ring is stronger than that in the chair-like N_6 hexazine ring (0.85), which results from the accommodation by the N_6 ring of excess electrons from Te. We employ the quantum theory of atoms in molecules (QTAIM) to quantify the number of transferred charges in TeN_6[55], and Bader charge analysis reveals that the N_6 hexazine ring accepts ~2.4 *e* from the nearly Te atoms. These electrons reside in the N–N antibonding π^* orbitals, prolongating the N–N bond length and weakening the N–N bonding, thereby decreasing the repulsion of lone electron pairs of N and finally stabilizing the distorted N_6 hexazine ring in TeN_6.

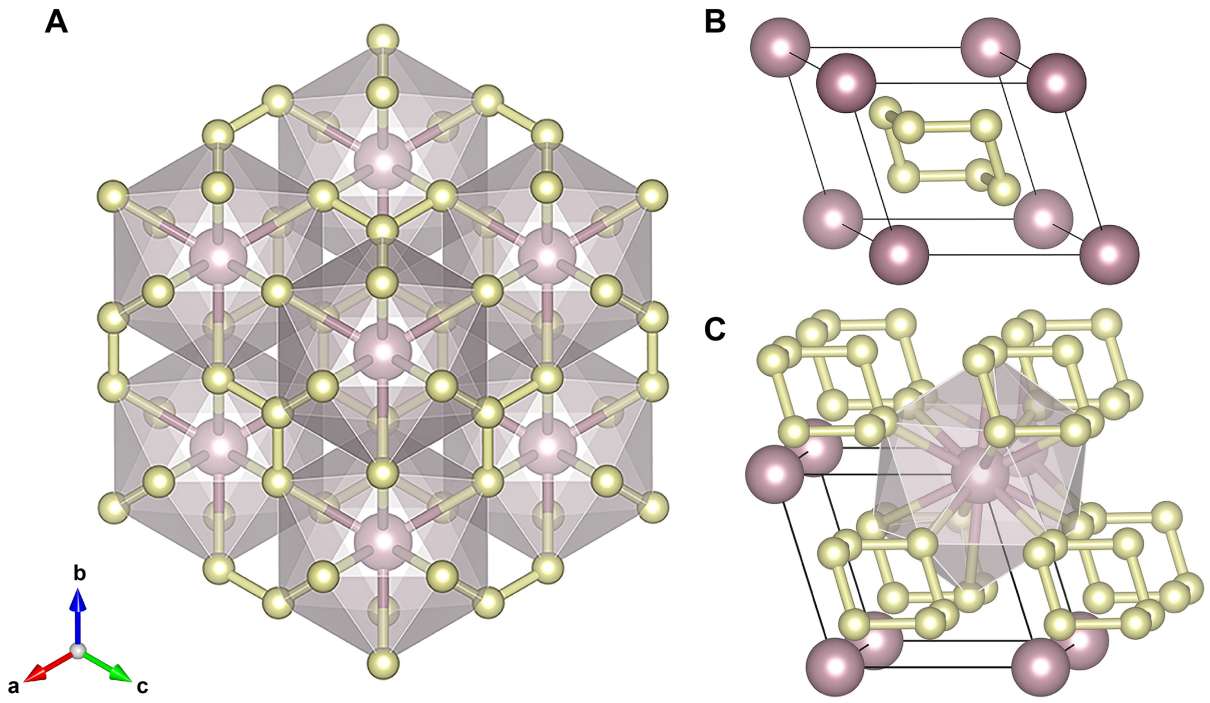

Figure 1. Crystal structure of 5*p*-block element nitrides MN_6 (M = Sb, Te, I). (A) MN_6 has *R*3*m* space group; (B) Rhombohedral primitive cell structure without showing any M–N bonds, and the chair-like N_6 hexazine ring is located in the center; (C) The hypercoordinated MN_{12} icosahedral cage. The large pink spheres and small yellow spheres represent the 5*p*-block elements and nitrogen, respectively.

The stable TeN_6 exhibits metallic features, corresponding to two distinct bands (labeled band I and band II) crossing the Fermi level (E_F) and dispersing from about 2 eV below E_F to 3 eV above E_F in the electron band structures [Figure 2B]. The projected density of states (PDOS) shows that the N atoms make a substantial contribution to the conduction bands [Figure 2C]. Moreover, obvious hybridizations between N and Te 5*s*, 5*p*, and 5*d* orbitals near the E_F indicate that in addition to the 5*s* and 5*p* electrons of Te, the pressure-induced 5*d* electrons also participate in the chemical bonding of nitrogen-rich compound TeN_6. The calculated COHP is displayed in Figure 2D, in which the fully occupied bonding states and partially occupied antibonding states lend strong support to the N–Te 5*s*, N–Te 5*p*, and N–Te 5*d* covalent bonding within the TeN_6. Therefore, Te not only has the basic properties of typical 5*p*-block elements but also exhibits electron occupation characteristics similar to those of *d*-block transition metal elements under high pressure.

In fact, a primitive cell of TeN_6 can be seen as composed of a N_6 hexazine ring and a Te atom [Figure 1B] llyy; its electron band structure near the E_F is modified from N_6 due to the hybridization between N and Te 5*s*, 5*p*, and 5*d* orbitals. Supplementary Figure 3 presents the electronic band structure of Te_0N_6, where two conduction bands are half-filled. The introduction of Te adds approximately two electrons to the N_6 hexazine ring, partially occupying the degenerate band near the E_F in TeN_6 [Figure 2B]. The occupancy of the degenerate band causes the electronic state to have orbital degeneracy, which is affected by the Jahn-Teller effect (JTE). Conventional JTE involves the coupling of electron and nuclear degrees of freedom and states that stability and degeneracy are not possible simultaneously unless all the nuclei in the equilibrium configuration lie on a straight line[56]. In short, the orbitally degenerate state means potential instability that causes the spontaneous distortion characteristic of the JTE[57]. Herein, the N_6 hexazine ring undergoes structural distortion and reduces the symmetry of the original configuration (from a planar ring with D_{6h}

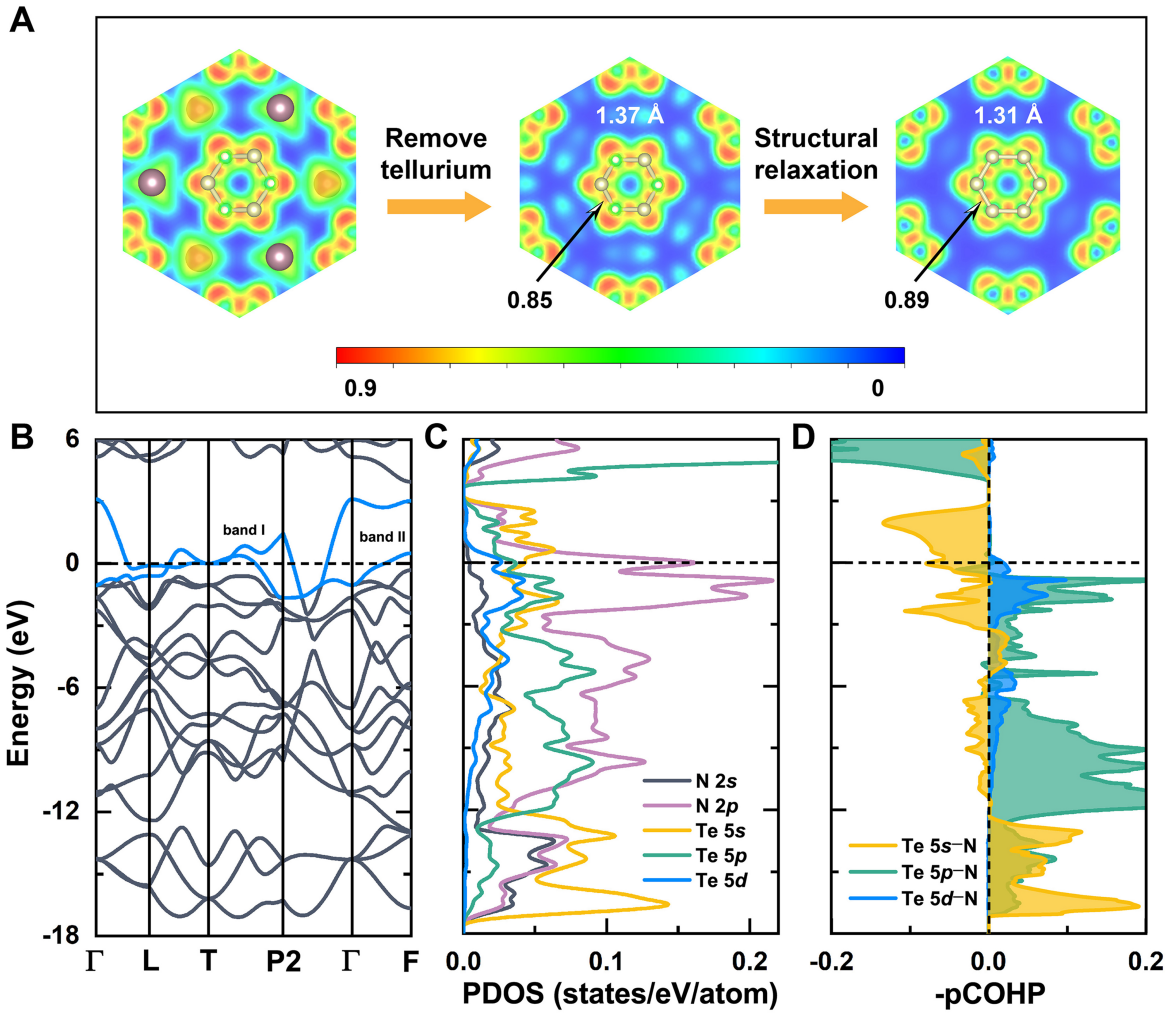

Figure 2. Electronic structures and chemical bonding of TeN_6. (A) ELF of TeN_6 (left), Te_0N_6 (middle), and relaxed N_6 hexazine ring (right). Its value ranges from 0 to 1, and the closer to 1, the stronger the electron localization, corresponding to the region of bonding and the lone electron pairs; (B) Electron band structure; (C) PDOS; (D) pCOHP of Te–N pairs, the negative and positive -pCOHP values denote antibonding and bonding interactions, respectively. Horizontal dotted lines indicate the Fermi level. ELF: electron localization function; PDOS: projected density of states; pCOHP: projected crystal orbital Hamilton population.

symmetry to a chair-like ring with D_{3d} symmetry), thereby lifting the orbital degeneracy and enhancing the structural stability. It is worth mentioning that the dynamic JTE is particularly favorable for superconductivity, which has been employed to explain the superconductivity in high-pressure hydride cI14-CaH_6 and B-doped diamond[58,59]. Furthermore, a Van Hove singularity (VHS) near the E_F in the PDOS of TeN_6 [Figure 2C] corresponds to the flat band structure at L, but the bands passing through the E_F along the Γ–L and P2–Γ directions are steeping [Figure 2B]. The existence of the VHS and Flat/Steep band indicates that TeN_6 may be a potential high-temperature superconductor.

To investigate this possibility, EPC calculations were performed for the nitrogen-rich compound TeN_6 at 100 GPa. The phonon dispersion results are depicted in Figure 3A; the absence of imaginary frequencies in the entire Brillouin zone indicates the dynamical stability of this compound. Two gaps separated the phonon dispersion curves into three regions [Figure 3B]: the low-frequency acoustic branches are associated with the lattice vibrations of Te owing to its large atomic mass (0~215 cm^{-1}), the high-frequency optical

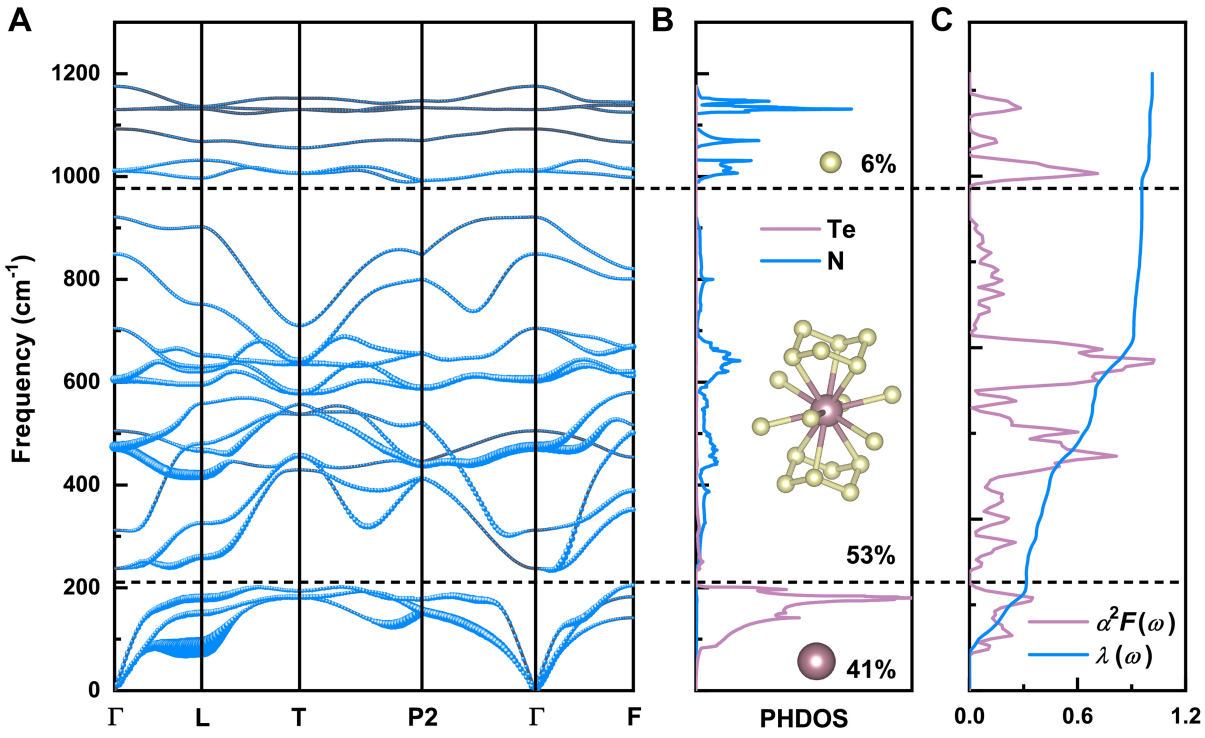

Figure 3. EPC in TeN_6. (A) Phonon dispersion curve. Blue circles represent the *q*-resolved EPC parameter $\lambda_{q,i}$ the radii of circles are proportional to the strength; (B) PHDOS. The illustrations and percentages are the contribution of the vibration modes to the EPC parameter λ; (C) Eliashberg spectral function $\alpha^2F(\omega)$ and integral EPC parameter $\lambda(\omega)$ as a function of frequency. EPC: electron-phonon coupling; PHDOS: phonon density of states.

branches correspond to the vibrations of N atoms (980~1180 cm^{-1}), whereas the mid-lying region is attributed to the strong interaction between Te and N atoms. By analyzing the Eliashberg spectral function $\alpha^2F(\omega)$, it can be concluded that the combined contribution of three regions (6%, 53%, and 41%, respectively) gave an EPC parameter λ of 1.01 [Figure 3C]. The vibration of the mid-frequency region plays a dominant role in EPC, which is derived primarily from the twofold degenerate E_g modes along the Γ–P2 direction (474 cm^{-1} and 605 cm^{-1}). Incidentally, these bands are the rock and breathing vibrations between I and N atoms, leading to the distortions in the N_6 hexazine ring structure. In addition, the contribution of lattice vibrations in the low-frequency region cannot be ignored, which will be discussed later. Superconducting critical temperature T_c is evaluated through the following Allen-Dynes modified McMillan equation[60]:

$$T_c = \frac{\omega_{log}}{1.2}\exp\left[-\frac{1.04(1+\lambda)}{\lambda-\mu^*(1+0.62\lambda)}\right],$$

where the ω_{log} is calculated logarithmic average phonon frequency, and μ^* is Coulomb pseudopotential. At 100 GPa, the predicted T_c of nitrogen-rich compound TeN_6 reaches 36.8 K, close to the McMillan limit (40 K). The EPC calculations are also performed for 125 GPa and 150 GPa, and the pressure evolution of

important parameters involved with the superconductivity of TeN_6 are displayed in Supplementary Table 3. There is a negative pressure dependence of T_c (28.6 K at 125 GPa and 20.8 K at 150 GPa), with a pressure coefficient (dT_c/dP) of -0.31 K/GPa.

A positive correlation between λ and T_c indicates that λ dominates the superconductivity of the nitrogen-rich compound TeN_6 [Figure 4A]. To elucidate the underlying superconducting mechanism, we extend the calculation of λ by adopting the simplified Hopfield expression[60]:

$$\lambda = \eta \cdot N(\varepsilon_F) = \frac{N(\varepsilon_F) I^2}{M\omega^2},$$

where η is the Hopfield parameter, $N(\varepsilon_F)$ is the electronic density of states (DOS) at E_F, I is the average electron-phonon matrix element, and $M\omega^2$ is the average lattice force constant. In this way, the EPC is separated into the lattice-related Hopfield parameter and a purely electron-related contribution given by the DOS.

Firstly, the lattice-related Hopfield parameter η decreases with the increase of pressure (0.15 at 100 GPa and 0.10 at 150 GPa), which is consistent with the evolution of λ [Supplementary Table 3]. Comparing the phonon dispersion curves under different pressures shows a striking feature that there is an obvious phonon softening in the low-frequency acoustic branches [Figure 4B], mainly near the L point and Γ–P2 direction. Furthermore, the q-resolved λ_q is particularly strong in these softened regions [Figure 3A], indicating that soft phonon mode is beneficial to enhance EPC. In order to clearly uncover the reason for the phonon softening, we assess the Fermi surface (FS) properties in rhombohedral TeN_6 at high pressure. The three-dimensional FS is mapped at 100 GPa using Fermisurfer, and the nesting function $\xi(q)$ is applied to describe the FS nesting (FSN). The $\xi(q)$ in Figure 4C quantifies the overlap of FS with an image of itself shifted by a vector q[60]:

$$\xi(q) = \frac{1}{N}\sum_{k,n,m} \delta(\varepsilon_{k,n} - \varepsilon_F)\,\delta(\varepsilon_{k+q,m} - \varepsilon_F),$$

where N is the number of k points, n and m are the indices of energy bands, and $\varepsilon_{k,n}$ is the Kohn-Sham eigenvalue. As shown in Figure 4D, a wave vector q connects two parallel FS pockets along the Γ–P2 direction, labeled as a black arrow in the cross-section, which usually represents effective nesting. The calculated $\xi(q)$ exhibits a strong feature (sharp peak) along the Γ–P2 direction with the exception of the maximum at Γ point (q = 0), demonstrating the occurrence of FSN, and this FSN disappears with increasing pressure from 100 GPa to 150 GPa [Figure 4C]. Surprisingly, the nesting direction corresponds to the phonon softening region, so it can be concluded that the soft phonon modes induced by FSN contribute to strong EPC of the nitrogen-rich compound TeN_6.

Next, we study the purely electron-related contribution to the EPC. As shown in [Figure 4E], the electronic DOS $N(\varepsilon_F)$ gradually decreases with increasing pressure. Due to the hybridizations between N and Te 5*s*, 5*p*, and 5*d* orbitals near the E_F, we quantify the occupied states of electrons at E_F to further analyze the

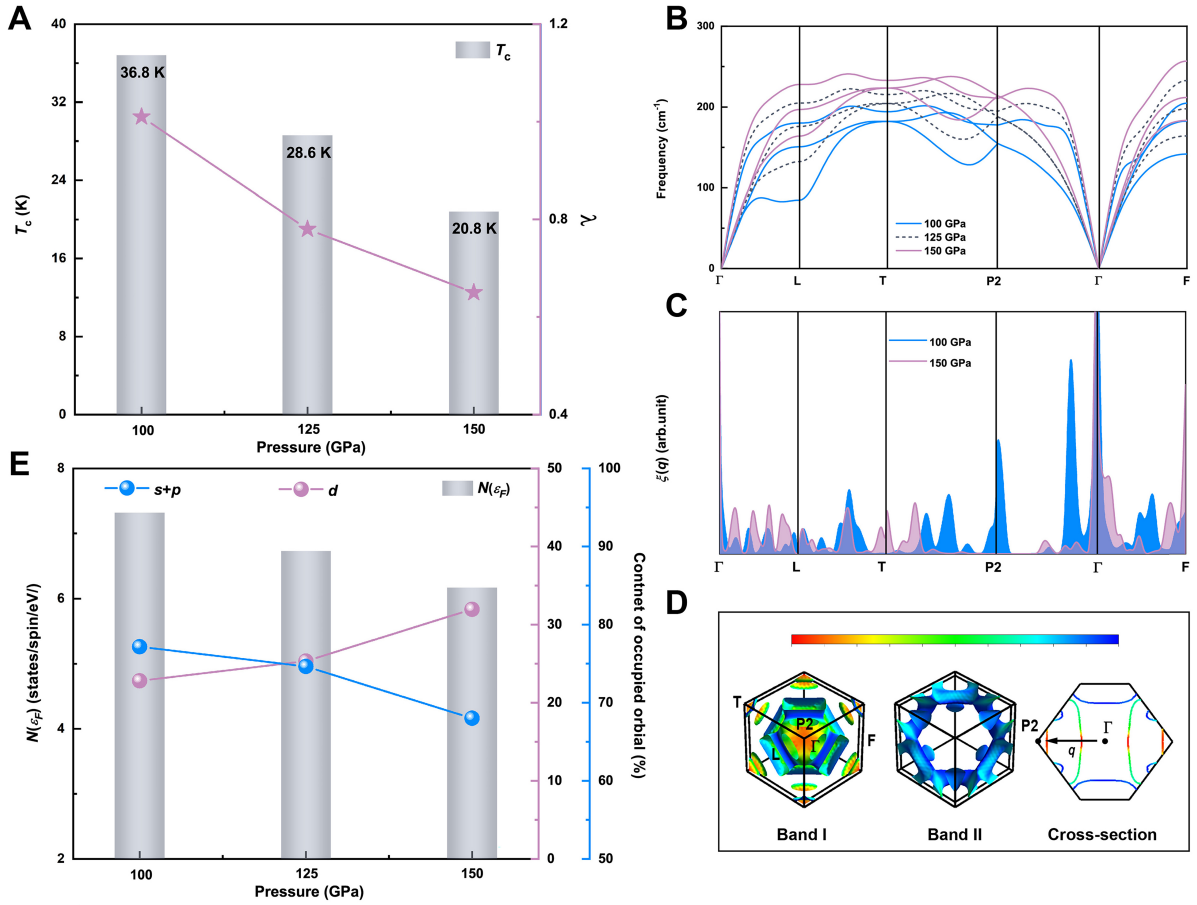

Figure 4. Superconductive mechanisms of TeN_6. (A) Calculated pressure variation of superconducting critical temperature T_c and EPC parameter λ; (B) Phonon dispersion curves at different pressures; (C) Fermi surface nesting function $\xi(q)$ along special q trajectories; (D) Three-dimensional Fermi surface and the cross-section at 100 GPa. The color bar represents the Fermi velocity on the Fermi surface; it makes blue as the minimum and red as the maximum. FSN occurs along the Γ–P2 direction (black arrow); (E) Pressure-induced variations of electronic DOS $N(\varepsilon_F)$. Red and blue spheres represent the content of 5*s*, 5*p*, and 5*d* occupied orbitals in the IPDOS of atomic Te at Fermi level (*s*+*p*% and *d*%). FSN: fermi surface nesting; DOS: density of states; IPDOS: integral projected density of states.

contribution of these hybridized electronic states to the EPC. The integral PDOS (IPDOS) in Supplementary Figure 4 shows that the total number of electronic states occupied by atomic Te at E_F gradually increases under compression, and the content of occupied 5*s*, 5*p*, and 5*d* states is quite different. Among them, the content of pressure-induced 5*d* states (*d*%) has a steady increase, while that of the 5*s* and 5*p* states (*s*+*p*%) shows a decreasing trend [Figure 4E]. The greater the content of pressure-induced 5*d* states, the more hybridized electronic states between N and Te 5*d* orbitals, significantly enhancing the covalent bonding between them. Integrated COHP (ICOHP) is used to quantitatively describe the bonding strength. The ICOHP value of Te 5*d*–N is negative, and its absolute value increases under compression [Supplementary Table 4]. This means that the covalent bonding between N and Te 5*d* orbitals gradually strengthens, contributing to the stability of the high-pressure nitrogen-rich compound TeN_6. However, the pressure dependence (positive) is opposite to that of λ (negative), hindering the improvement of EPC. Consequently, the strong EPC in nitrogen-rich compound TeN_6 mainly originates from the hybridized electronic states between N and Te 5*s* and 5*p* orbitals; the pressure-induced 5*d* electron of Te weakens the EPC and depresses the superconductivity.

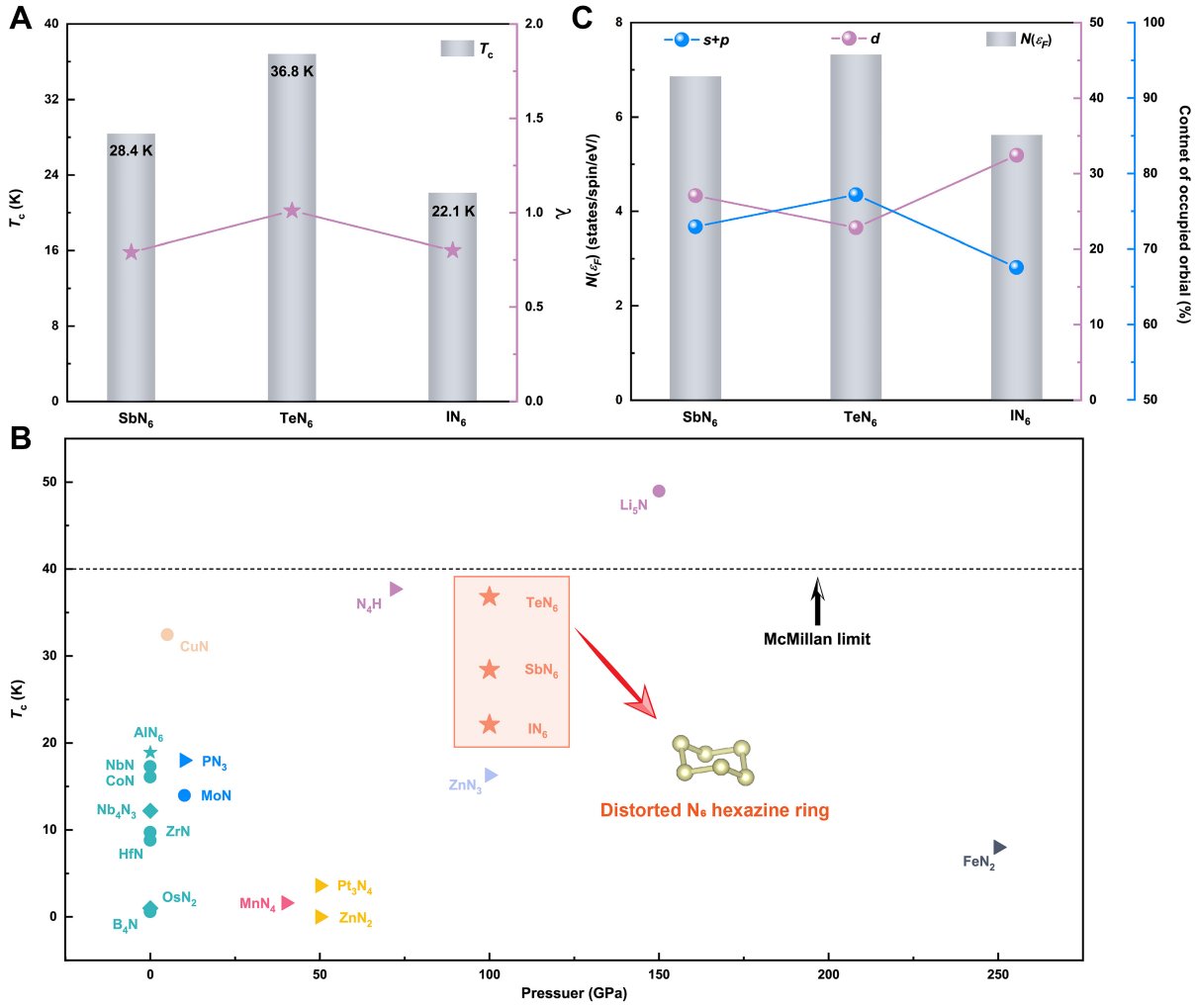

Figure 5. Formation mechanism of nitrogen-based superconductors MN_6 (M = Sb, Te, I). (A) Calculated T_c and EPC parameter λ at 100 GPa; (B) The superconductivity dependence on pressure of the reported binary superconducting nitrides including SbN_6, TeN_6, and IN_6 proposed in this work; (C) Electronic DOS $N(\varepsilon_F)$ and the content of occupied orbitals in the IPDOS of 5*p*-block element at Fermi surface. Red and blue spheres represent the 5*s*, 5*p*, and 5*d* orbitals, respectively. EPC: electron-phonon coupling; DOS: density of states; IPDOS: integral projected density of states.

The 5*p*-block elements successfully polymerize the nitrogen into the metallic and superconductive N_6 hexazine ring, opening a new avenue for further enlarging and enriching polynitrogen arrangements under compression. Unsurprisingly, Sb and I, located in the same period as Te, can also induce the superconductivity of the distorted N_6 hexazine ring [Supplementary Figures 5 and 6]; the resulting critical temperatures of SbN_6 and IN_6 are 28.4 K and 22.1 K, respectively [Figure 5A]. To the best of our knowledge, this is the first time to predict the nitrogen-based superconductor with N_6 rings, and the T_c is the highest among the known nitrides with ring-like polynitrogen structure [Figure 5B and Supplementary Table 5]. The associated EPC properties of MN_6 (M = Sb, Te, I) are listed in Supplementary Table 3, and the difference in superconducting behavior among these nitrogen-rich compounds with the same stoichiometry mainly stems from the electronic DOS at E_F. From the PDOS in Supplementary Figure 7, one can see that the 5*d* orbitals of Sb and I also hybridize with N near the E_F, which directly proves that high pressure effectively activates the vacant 5*d* orbital of 5*p*-block elements, making them participate in chemical bonding together with the 5*s* and 5*p* orbitals. The covalent bonding characteristics of the M–N bonds can be

observed from the COHP and the ELF in Supplementary Figures 8 and 9. By projecting the electron band structure onto the pressure-induced 5*d* orbitals, we find that the contribution of the 5*d* orbital at E_F does not change monotonically with increasing atomic number [Supplementary Figure 10], so the T_c of different M N_6 compounds may be related to these pressure-induced 5*d* states. To verify this conjecture, the occupied states of electrons of 5*p*-block elements at E_F are quantified, and the results are shown in Figure 5C. Te has the lowest content of 5*d* states, but TeN_6 has the highest T_c, elucidating that the pressure-induced 5*d* electron is negatively correlated with the superconductivity of 5*p*-block element nitrides.

CONCLUSIONS

Using first-principles calculations, the first nitrogen-based superconductor with the distorted N_6 hexazine ring is designed at high pressure. The 5*p*-block element acts as precompressors and electron donors for the N sublattice, resulting in Jahn-Teller distortion of the N_6 hexazine ring and endowing the 5*p*-block element nitrides a T_c up to 36.8 K at 100 GPa. This critical temperature, close to the McMillan limit, is attributed to the strong EPC caused by the phonon softening and the hybridized electronic states between N and 5*s* and 5*p* orbitals of the 5*p*-block element. The discovery of metallic and even superconducting N_6 hexazine ring in the 5*p*-block element nitrides provides new insights into achieving the metallization of solid nitrogen at high pressure. Moreover, our present works open an avenue for further exploring many other *p*-block element nitrides, enriching nitrogen chemistry under extreme conditions.

DECLARATIONS

Authors' contributions

Conception, design, writing, and editing: Liu Y, Li D
DFT calculation and data collection: Liu Y
Data analysis and interpretation: Liu Y, Li D
Revision of articles: Li D, Cui T

Availability of data and materials

Not applicable.

Financial support and sponsorship

This work was supported by the National Key R&D Program of China (No. 2023YFA1406200), the National Natural Science Foundation of China (No. 12374004 and No. 12174141), and the High Performance Computing Center of Jilin University, China.

Conflicts of interest

All authors declared that there are no conflicts of interest.

Ethical approval and consent to participate

Not applicable.

Consent for publication

Not applicable.

REFERENCES

1. Adeleke AA, Greschner MJ, Majumdar A, et al. Single-bonded allotrope of nitrogen predicted at high pressure. *Phys Rev B* 2017;96:224104. DOI
2. Laniel D, Geneste G, Weck G, Mezouar M, Loubeyre P. Hexagonal layered polymeric nitrogen phase synthesized near 250 GPa. *Phys Rev Lett* 2019;122:066001. DOI PubMed
3. Hirshberg B, Gerber RB, Krylov AI. Calculations predict a stable molecular crystal of N_8. *Nat Chem* 2014;6:52-6. DOI PubMed
4. Wang X, Wang Y, Miao M, et al. Cagelike diamondoid nitrogen at high pressures. *Phys Rev Lett* 2012;109:175502. DOI PubMed
5. Mattson WD, Sanchez-Portal D, Chiesa S, Martin RM. Prediction of new phases of nitrogen at high pressure from first-principles simulations. *Phys Rev Lett* 2004;93:125501. DOI PubMed
6. Zahariev F, Dudiy SV, Hooper J, Zhang F, Woo TK. Systematic method to new phases of polymeric nitrogen under high pressure. *Phys Rev Lett* 2006;97:155503. DOI PubMed
7. Kotakoski J, Albe K. First-principles calculations on solid nitrogen: a comparative study of high-pressure phases. *Phys Rev B* 2008;77:144109. DOI
8. Alemany MMG, Martins JL. Density-functional study of nonmolecular phases of nitrogen: metastable phase at low pressure. *Phys Rev B* 2003;68:024110. DOI
9. Wang X, Tian F, Wang L, et al. Predicted novel metallic metastable phases of polymeric nitrogen at high pressures. *New J Phys* 2013;15:013010. DOI
10. Jiang S, Holtgrewe N, Lobanov SS, et al. Metallization and molecular dissociation of dense fluid nitrogen. *Nat Commun* 2018;9:2624. DOI PubMed PMC
11. Bergermann A, Redmer R. Nonmetal-to-metal transition in dense fluid nitrogen at high pressure. *Phys Rev B* 2023;108:085101. DOI
12. Steele BA, Stavrou E, Crowhurst JC, Zaug JM, Prakapenka VB, Oleynik II. High-pressure synthesis of a pentazolate salt. *Chem Mater* 2017;29:735-41. DOI
13. Laniel D, Winkler B, Koemets E, et al. Synthesis of magnesium-nitrogen salts of polynitrogen anions. *Nat Commun* 2019;10:4515. DOI PubMed PMC
14. Bykov M, Bykova E, Aprilis G, et al. Fe–N system at high pressure reveals a compound featuring polymeric nitrogen chains. *Nat Commun* 2018;9:2756. DOI PubMed PMC
15. Zhai H, Xu R, Dai J, et al. Stabilized Nitrogen Framework Anions in the Ga–N System. *J Am Chem Soc* 2022;144:21640-7. DOI
16. Ceppatelli M, Serrano-Ruiz M, Morana M, et al. High-pressure and high-temperature synthesis of crystalline Sb_3N_5. *Angew Chem Int Ed Engl* 2024;63:e202319278. DOI
17. Sangiovanni DG, Faccio R, Gueorguiev GK, Kakanakova-Georgieva A. Discovering atomistic pathways for supply of metal atoms from methyl-based precursors to graphene surface. *Phys Chem Chem Phys* 2022;25:829-37. DOI PubMed
18. Aslandukov A, Trybel F, Aslandukova A, et al. Anionic N_{18} macrocycles and a polynitrogen double helix in novel yttrium polynitrides YN_6 and Y_2N_{11} at 100 GPa. *Angew Chem Int Ed Engl* 2022;61:e202207469. DOI PubMed PMC
19. Bykov M, Chariton S, Fei H, et al. High-pressure synthesis of ultraincompressible hard rhenium nitride pernitride $Re_2N(_2)(N)_2$ stable at ambient conditions. *Nat Commun* 2019;10:2994. DOI PubMed PMC
20. Bykov M, Bykova E, Ponomareva AV, et al. Stabilization of polynitrogen anions in tantalum-nitrogen compounds at high pressure. *Angew Chem Int Ed Engl* 2021;60:9003-8. DOI
21. Bykov M, Chariton S, Bykova E, et al. High-pressure synthesis of metal-inorganic frameworks $Hf_4N_{20}{\cdot}N_2$, $WN_8{\cdot}N_2$, and $Os_5N_{28}{\cdot}3N_2$ with polymeric nitrogen linkers. *Angew Chem Int Ed Engl* 2020;59:10321-6. DOI PubMed PMC
22. Laniel D, Winkler B, Fedotenko T, et al. High-pressure $Na_3(N_2)_4$, $Ca_3(N_2)_4$, $Sr_3(N_2)_4$, and $Ba(N_2)_3$ featuring nitrogen dimers with noninteger charges and anion-driven metallicity. *Phys Rev Mater* 2022;6:023402. DOI
23. Yu S, Huang B, Zeng Q, Oganov AR, Zhang L, Frapper G. Emergence of novel polynitrogen molecule-like species, covalent chains, and layers in magnesium–nitrogen Mg_xN_y phases under high pressure. *J Phys Chem C* 2017;121:11037-46. DOI
24. Schneider SB, Frankovsky R, Schnick W. Synthesis of alkaline earth diazenides $M_{AE}N_2$ (M_{AE} = Ca, Sr, Ba) by controlled thermal decomposition of azides under high pressure. *Inorg Chem* 2012;51:2366-73. DOI PubMed
25. Zhang M, Yan H, Wei Q, Wang H, Wu Z. Novel high-pressure phase with pseudo-benzene "N_6" molecule of LiN_3. *EPL* 2013;101:26004. DOI
26. Wang X, Li J, Xu N, Zhu H, Hu Z, Chen L. Layered polymeric nitrogen in RbN_3 at high pressures. *Sci Rep* 2015;5:16677. DOI PubMed PMC
27. Huang B, Frapper G. Barium–nitrogen phases under pressure: emergence of structural diversity and nitrogen-rich compounds. *Chem Mater* 2018;30:7623-36. DOI
28. Zhang J, Zeng Z, Lin HQ, Li YL. Pressure-induced planar N_6 rings in potassium azide. *Sci Rep* 2014;4:4358. DOI PubMed PMC
29. Wang Y, Bykov M, Chepkasov I, et al. Stabilization of hexazine rings in potassium polynitride at high pressure. *Nat Chem* 2022;14:794-800. DOI
30. Laniel D, Trybel F, Yin Y, et al. Aromatic hexazine $[N_6]^{4-}$ anion featured in the complex structure of the high-pressure potassium nitrogen compound K_9N_{56}. *Nat Chem* 2023;15:641-6. DOI
31. Raza Z, Errea I, Oganov AR, Saitta AM. Novel superconducting skutterudite-type phosphorus nitride at high pressure from first-principles calculations. *Sci Rep* 2014;4:5889. DOI PubMed PMC

32. Li D, Tian F, Lv Y, et al. Stability of sulfur nitrides: a first-principles study. *J Phys Chem C* 2017;121:1515-20. DOI
33. Wang W, Wang H, Liu Y, et al. High-pressure bonding mechanism of selenium nitrides. *Inorg Chem* 2019;58:2397-402. DOI
34. Wang L, Sun R, Liu W, et al. Novel superhard boron-rich nitrides under pressure. *Sci China Mater* 2020;63:2358-64. DOI
35. Dong X, Oganov AR, Cui H, Zhou XF, Wang HT. Electronegativity and chemical hardness of elements under pressure. *Proc Natl Acad Sci U S A* 2022;119:e2117416119. DOI PubMed PMC
36. Peng F, Wang Y, Wang H, Zhang Y, Ma Y. Stable xenon nitride at high pressures. *Phys Rev B* 2015;92:094104. DOI
37. Zhao Y, Gao J, Zhang X, Ding S, Liu Y, Yang G. Superconducting $Li_{11}Sb_2$ electride at ambient pressure. *J Mater Chem C* 2023;11:17087-92. DOI
38. Gao Y, Cui T, Li D. Unexpected *d*−*p* orbital covalent interaction between the non-*d*-block main-group metal tellurium and fluorine at high pressure. *Fund Res* 2023;In Press. DOI
39. Luo D, Lv J, Peng F, et al. A hypervalent and cubically coordinated molecular phase of IF_8 predicted at high pressure. *Chem Sci* 2019;10:2543-50. DOI PubMed PMC
40. Gonze X, Lee C. Dynamical matrices, Born effective charges, dielectric permittivity tensors, and interatomic force constants from density-functional perturbation theory. *Phys Rev B* 1997;55:10355-68. DOI
41. Kohn W, Sham LJ. Self-consistent equations including exchange and correlation effects. *Phys Rev* 1965;140:A1133. DOI
42. Perdew JP, Wang Y. Accurate and simple analytic representation of the electron-gas correlation energy. *Phys Rev B Condens Matter* 1992;45:13244-9. DOI PubMed
43. Perdew JP, Burke K, Ernzerhof M. Generalized gradient approximation made simple. *Phys Rev Lett* 1996;77:3865-8. DOI PubMed
44. Kresse G, Joubert D. From ultrasoft pseudopotentials to the projector augmented-wave method. *Phys Rev B* 1999;59:1758-75. DOI
45. Momma K, Izumi F. *VESTA 3* for three-dimensional visualization of crystal, volumetric and morphology data. *J Appl Crystallogr* 2011;44:1272-6. DOI
46. Kresse G, Furthmüller J. Efficient iterative schemes for ab initio total-energy calculations using a plane-wave basis set. *Phys Rev B Condens Matter* 1996;54:11169-86. DOI PubMed
47. Kutzelnigg W. Chemical bonding in higher main group elements. *Angew Chem Int Ed Engl* 1984;23:272-95. DOI
48. Kawamura M. FermiSurfer: Fermi-surface viewer providing multiple representation schemes. *Comput Phys Commun* 2019;239:197-203. DOI
49. Giannozzi P, Baroni S, Bonini N, et al. QUANTUM ESPRESSO: a modular and open-source software project for quantum simulations of materials. *J Phys Condens Matter* 2009;21:395502. DOI
50. Allen PB. Neutron spectroscopy of superconductors. *Phys Rev B* 1972;6:2577-9. DOI
51. Liu Z, Li D, Zhuang Q, et al. Formation mechanism of insensitive tellurium hexanitride with armchair-like cyclo-N_6 anions. *Commun Chem* 2020;3:42. DOI PubMed PMC
52. Liu Y, Wang R, Wang Z, Li D, Cui T. Formation of twelve-fold iodine coordination at high pressure. *Nat Commun* 2022;13:412. DOI PubMed PMC
53. Ha TK, Cimiraglia R, Nguyen MT. Can hexazine (N_6) be stable? *Chem Phys Lett* 1981;83:317-9. DOI
54. Huber H. Is hexazine stable? *Angew Chem Int Ed Engl* 1982;21:64-5. DOI
55. Bader RFW. Atoms in molecules: a quantum theory. Oxford: Clarendon; 1990. Available from: https://global.oup.com/academic/product/atoms-in-molecules-9780198558651?cc=us&lang=en&. [Last accessed on 21 Mar 2024].
56. Jahn HA, Teller E. Stability of polyatomic molecules in degenerate electronic states - I - Orbital degeneracy. *Proc R Soc Lond A* 1937;161:220-35. DOI
57. Weger M, Englman R. A dynamic Jahn-Teller theory for high-T_c superconductivity. *Physica A* 1990;168:324-37. DOI
58. Wang H, Tse JS, Tanaka K, Iitaka T, Ma Y. Superconductive sodalite-like clathrate calcium hydride at high pressures. *Proc Natl Acad Sci U S A* 2012;109:6463-6. DOI PubMed PMC
59. Ma Y, Tse JS, Cui T, et al. First-principles study of electron-phonon coupling in hole- and electron-doped diamonds in the virtual crystal approximation. *Phys Rev B* 2005;72:014306. DOI
60. Allen PB, Dynes RC. Transition temperature of strong-coupled superconductors reanalyzed. *Phys Rev B* 1975;12:905-22. DOI
61. Mcmillan WL. Transition temperature of strong-coupled superconductors. *Phys Rev* 1968;167:331-44. DOI
62. Ma Y, Duan D, Shao Z, et al. Divergent synthesis routes and superconductivity of ternary hydride $MgSiH_6$ at high pressure. *Phys Rev B* 2017;96:144518. DOI